IRAQI JOURNAL OF APPLIED PHYSICS
Vol. 22, No. 1, January-March 2026, pp. 145-152

Optimization of Si/SiGe HBT Architecture Integrated in 28-nm FD-SOI BiCMOS Technology

Chems E. Lachkhab *
Maya Lakhdara
Yasser Mansouri
Saida Latreche

Laboratoire Hyperfréquences et Semi-conducteurs (LHS),
Faculté des Sciences de la Technologie,
Université Frères Mentouri Constantine 1,
Constantine 25000, ALGERIA
*Corresponding author:
chemselghizlane.lachkhab@doc.umc.edu.dz

This work aims to investigate a new Si/SiGe HBT in the fully depleted silicon on insulator technology (FD-SOI 28 nm). The epitaxial extrinsic base isolated from the collector (EXBIC) architecture has been used in this technology to reduce base resistance and enable cut-off frequencies to exceed 400 and 600 GHz for transition frequency f_t and maximum oscillation frequency f_{max}, respectively. Static and dynamic characteristics of the FD-SOI 28 nm have been evaluated using COMSOL multiphysics software. The technology achieved at base-emitter voltage of 0.83V, a value of 346 and 763.35 GHz for f_t and f_{max}, respectively. To further enhance frequency performance, architecture parameters such as germanium concentration, extrinsic base doping, emitter height and width are optimized achieving f_t of 360 GHz and f_{max} of 900 GHz. The results demonstrate the potential of using the SiGe HBTs based on the FD-SOI technology in the RF modules and THz systems.

Keywords: Silicon devices; SiGe structures; Bipolar transistors; BiCMOS technology; COMSOL
Received: 7 July; Revised: 24 September; Accepted: 1 October 2025; Published: 1 January 2026

1. Introduction

The growing demands of customers in micro and nanotechnology industries, modern wireless communications systems accentuates the development of fundamental component capable of operating at higher frequencies [1,2]. Currently, electronic devices are fabricated with high cut-off frequencies exceeding 370 GHz, facilitating their applications in the millimeter-wave and THz bands [3,4].

BiCMOS technologies are particularly attractive for these type of applications due to their ability to combine high integration, high performance and low cost [5]. Among the various options, components based on heterojunction structures stand out as the most promising candidates for achieving the required functional frequencies while maintaining low noise levels [6]. The creation of Si/SiGe HBT technologies are known for their ability to reach performance frequencies in the terahertz range, offering significant potential for the development of ultra-fast electronic circuits. SiGe alloys are especially well-suited for these devices due to their narrower bandgap compared to pure silicon. Introducing SiGe alloys into the base of HBT's makes it feasible to modify the silicon energy bands [7-9].

The transistor architecture is a key factor in performance enhancement. One of the most widely adopted self-aligned architecture is the Double Polysilicon Self-Aligned (DPSA), which uses Selective Epitaxial Growth of the base (SEG). This architecture has been used and developed by STMicroelectronics in BiCMOS 55nm technology, achieving transition frequency f_t of 320 GHz and maximum oscillation frequency f_{max} of 380 GHz [10,11]. However, the BiCMOS55 suffers from high extrinsic base resistance, which remains the primary limitation in achieving better performance compared to the transistor of IHP, which reaches for the same node a maximum frequency of 570 GHz. To overcome these limitations and to improve frequency performances, beyond 600 GHz and 400 GHz for maximum and transition frequency, a new technology of SiGe HBT integrated on fully depleted silicon on insulator FD-SOI, with an emitter width of 28 nm, has been developed. The FD-SOI 28 nm technology is manufactured based on Epitaxial eXtrinsic base isolated from the Collector (EXBIC) architecture, which is built on two important features: (i) an epitaxial boron in-situ-doped lateral base link reduces the extrinsic base resistance, (ii) an isolation (buried oxide layer BOX) implanted between the extrinsic base and the collector. The latter prevents boron diffusion and reduces the base collector capacitance; and also, offers the ability to control the collector profile using an intrinsic in-situ doped collector [12,13].

The main purpose of adding the buried oxide (BOX) is to provide a solution with high performance and low power consumption. This is achieved by electrically isolating the extrinsic base from the collector via the BOX layer, which significantly decreases the base-collector capacitance C_{BC}. As demonstrated in [12], increasing the BOX layer thickness leads to a significant decrease in C_{BC} , resulting in a marked improvement in both transition frequency f_t and maximum frequency f_{max}.

IRAQI JOURNAL OF APPLIED PHYSICS
Vol. 22, No. 1, January-March 2026, pp. 145-152

Compared to silicon bulk, the SOI technology frequently offers 20 to 30 % better performance at the same operating voltage. These advantages make the technology based on SOI layer particularly attractive for high performance applications including wireless communication, radar and THz systems [14].

In order to further enhance the electrical performance of FD-SOI 28 nm technology, particularly the frequency f_t and f_{max}, an optimization of electrical parameters is the main purpose of this work. The first part of this paper describes the architecture used in the FD-SOI 28 nm technology and its electrical performance. The simulation results enable a review of static and dynamic characteristics, including base and collector currents (I_C, I_B), static gain (β), transition and maximum oscillation frequency (f_t and f_{max}). Furthermore, a comparison of the frequency performance between the studied technology and the BiCMOS55 was performed to better evaluate the impact of the EXBIC architecture. To validate our results, a comparative analysis was also conducted against results reported in the literature. The second part focuses on optimizing several electrical and geometrical parameters, such as germanium concentration x, extrinsic base doping N_{ab}, emitter height d_E and emitter width w_{fd}, to further enhance the cut-off frequency f_t and f_{max} before initiating the process trials.

This paper demonstrates significant potential for THz operation, confirming the suitability of the FD-SOI technology for advanced RF front-end integration. This study also provides valuable insights into the co-design of device geometry and technology parameters for next-generation SiGe HBTs in sub-THz applications.

2. Physical Design and Numerical Simulation

The investigated structure consists of NPN SiGe HBT integrated into the FD-SOI 28nm technology with a frequency performance of f_t/f_{max}= 380/780 GHz [15]. The device structure shown in Fig. (1) consists of a heavily-doped collector n^{++} ($3x10^{19}$ cm^{-3}), sandwiched between two shallow trench isolations STI, and an intrinsic collector (n) formed by selective epitaxial growth of arsenic doped silicon SIC with a doping of $7x10^{16}$ cm^{-3}. The base region is composed of a thin intrinsic SiGe base (30 nm) with a germanium concentration of 20% and a doping of $5x10^{18}$ cm^{-3}[16]. This layer is aligned with an extrinsic base composed of a polysilicium base and base link, which is more heavily doped ($4x10^{19}$ cm^{-3}). The emitter section is composed of two parts, a thin mono-silicon layer and relatively thicker polysilicon layer. The total height of the emitter is 90 nm and a Gaussian doping profile ranging from $2x10^{21}$ cm^{-3} to $9x10^{16}$ cm^{-3} (Fig. 2) [17]. The BOX layer in this structure is used to separate the extrinsic base to the extrinsic collector. In addition, oxide sidewalls are used between the selective implanted collector SIC and the extrinsic base, which avoid boron diffusion from the intrinsic base to the collector. As a result, reducing base-collector capacitance and extrinsic base resistance [13]. Table (1) summarized the main electrical parameters of the studied architecture.

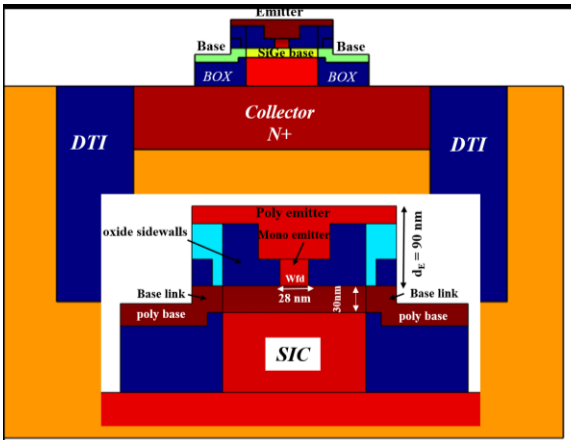

Fig. (1) The final structure of the EXBIC structure used in the 28nm FD-SOI technology under COMSOL software

Table (1) Electrical parameters of the SiGe HBT integrated in FD-SOI BiCMOS 28nm

Region	Emitter	Poly base	SiGe base	SIC	Collector
Height (nm)	90	45	30	90	200
Doping (cm^{-3})	$2x10^{21}$	$4x10^{19}$	$5x10^{18}$	$5x10^{16}$	$3x10^{19}$

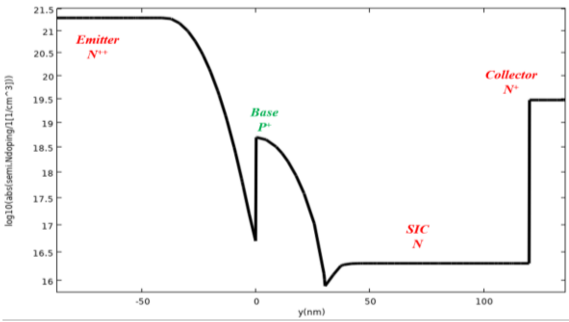

Fig. (2) Vertical doping profile of the FD-SOI 28nm under COMSOL

2.1. Simulation Models

In our study, the semiconductor Module of the COMSOL software, which is designed for simulating and analyzing semiconductor devices, has been used to simulate the electrical properties of the studied HBT. It provides a set of physics interfaces and features that enable detailed modeling of electrical, thermal, and quantum effects in semiconductor structures.

2.1.1. DDM model

The drift diffusion model DDM is a fundamental approach used to simulate charge transport in semiconductor devices. It combines the movement of electrons and holes caused by electric fields (drift) and concentration differences (diffusion), along with electrostatic effects described by Poisson's equation. This model couples Poisson's equation with the continuity equations for carriers, including generation and recombination effects.

Poisson's equation:

$$\nabla * (-\mathcal{E}_r * V * \nabla) = q(P - N + N_D^+ + N_A^-) \quad (1)$$

Electrons and holes continuity equations:

$$\frac{\partial N}{\partial t} = + \frac{1}{q}(\nabla \times J_n) - U_n \quad (2)$$

$$\frac{\partial P}{\partial t} = - \frac{1}{q}(\nabla \times J_p) - U_p \quad (3)$$

where N and P are the concentration of electron and hole, N_D^+ and N_A^- are the concentration of ionization of impurities and ε_r is the relative permittivity of the material

The rate net of electronic and hole recombination U_n and U_p are represented in equations (4) and (5), where R_n and R_p are the recombination rates for electrons and holes and, G_n and G_p are the generation rates of electrons and holes [18].

$$U_n = R_n - G_n \quad (4)$$

$$U_p = R_p - G_P \quad (5)$$

Equations (6) and (7) are derived from Maxwell:

$$J_n = +qN\mu_n \frac{d\phi_n}{d_x} \quad (6)$$

$$J_p = -qP\mu_p \frac{d\phi_p}{d_x} \quad (7)$$

The current densities J_n and J_p are depend of mobility of electron and hole μ_p and μ_n, and also the quasi-fermi potentials of the carriers ϕ_n and ϕ_p [19].

2.1.2. Mobility model

The Arora mobility model is the most widely used in COMSOL Multiphysics for semiconductor device simulation, as it accounts for both phonon scattering and ionized impurity scattering, unlike simpler models such as the power law model, which only consider phonon scattering. Arora model directly computes mobility from parameters such as doping and temperature without requiring additional external inputs, which makes it autonomous as a basis for mobility. This model thus offers a better accuracy for doped semiconductors, providing a more realistic estimate for heavily doped regions than a phonon-only model [20]. The general equation of this model are:

$$\mu_{n,ar} = \mu_{n,min} + \frac{\mu_{n0}}{1 + (\frac{N}{N_{n0}})(\frac{N}{N_{n0}})^{\alpha_n}} \quad (8)$$

$$\mu_{p,ar} = \mu_{p,min} + \frac{\mu_{p0}}{1 + (\frac{N}{N_{p0}})^{\alpha_p}} \quad (9)$$

with

$$N = N_a^- + N_d^+ \quad (10)$$

$$\mu_{n,min} = \mu_{n,min}^{ref}(\frac{T_l}{T_{ref}})^{\beta_1} \quad (11)$$

$$\mu_{p,min} = \mu_{p,min}^{ref}(\frac{T_l}{T_{ref}})^{\beta_1} \quad (12)$$

$$\mu_{n,0} = \mu_{n,0}^{ref}(\frac{T_l}{T_{ref}})^{\beta_2} \ , \ \mu_{p,0} = \mu_{p,0}^{ref}(\frac{T_l}{T_{ref}})^{\beta_2} \quad (13)$$

$$N_{n,0} = N_{n,0}^{ref}(\frac{T_l}{T_{ref}})^{\beta_3}, N_{p,0} = N_{p,0}^{ref}(\frac{T_l}{T_{ref}})^{\beta_3} \quad (14)$$

$$\alpha_{n,0} = \alpha_{n,0}^{ref}(\frac{T_l}{T_{ref}})^{\beta_4}, \alpha_{p,0} = \alpha_{p,0}^{ref}(\frac{T_l}{T_{ref}})^{\beta_4} \quad (15)$$

The various variables mentioned in the above system of equations: $\mu_{n,ar}$, $\mu_{p,ar}$ are Arora mobility of electron and hole. $\mu_{n,min}, \mu_{p,min}$ minimum mobility of electron and hole. μ_{n0}, μ_{p0} initial mobility, $\mu_{n,0}^{ref}$, $\mu_{p,0}^{ref}$ are the reference mobility. N, N_{n0} , N_{p0} , $N_{n,0}^{ref}$, $N_{p,0}^{ref}$ are concentration of dopants, electron impurities, hole impurities, electron and hole reference concentrations successively. T_1 , T_{ref} are the ambient and reference temperature. $\beta_1, \beta_2, \beta_3, \beta_4$ are the exponent of minimum reference mobility, reference mobility and reference impurity concentrations of coefficient α.

3. Electric Characteristics

3.1. Static Characteristics

Figure (3) shows gummel plots and static gain as a function of base-emitter voltage V_{BE}, varying from 0 to 1.1 V, while the base-collector voltage V_{BC} is fixed at 1.5 V. These graphs allow for a rapid evaluation of the ideality of the transistor currents, as indicated by the differences between the various curves. They also emphasize quasi-saturation effects, which are caused by high series resistance values [16]. At low injection regime ($V_{BE} < 0.4$V), the base current I_B is influenced by recombination phenomena at the space charge zone. Consequently, only a small number of electrons reach the base, resulting in fewer charges in the collector. This is revealed on the curve by a very low base and collector currents, as well as a correspondingly low current gain. In the normal operating regime ($0.4V<V_{BE}<0.8V$), electron injection becomes sufficient to cross the base and reach the collector, the transistor exhibits amplifying behavior and the gap between the collector and base currents curves represents the static current gain. The linear variation of the currents with V_{BE} allows for the extraction of saturation currents and the ideality factors of the junctions, for $V_{BE} = 0.55$ V the transistor achieves its maximum static gain of β_{max}= 3742. At high carrier injection ($V_{BE} > 0.8$V), the current gain is significantly reduced due to the Kirk effect, which corresponds to a change in the electric field at the collector junction. The collector current density rises above the collector doping concentration due to the increased electron injection from the emitter into the base. This condition causes a reduction in the electric field in the space charge region between base and collector, which normally prevents hole diffusion out of the base. As the field decreases, the hole profile extends toward the collector, forming a quasi-neutral region and leading to a virtual increase of the base thickness. This base enlargement results in a significant degradation in current gain [21].

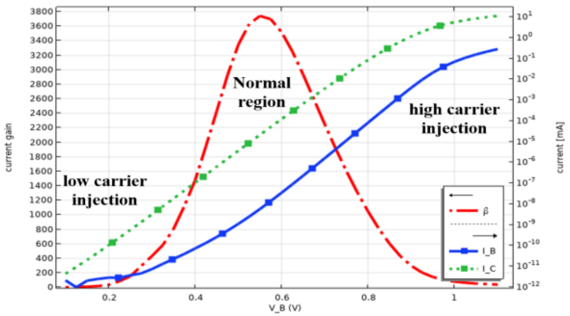

Fig. (3) Variation of I_B, I_C and β as a function of V_{BE} of the FD-SOI28nm

Figure (4) presents the output characteristics I_C (V_{CE}) with different values of base current I_B (1µA, 2µA, 3µA). It can be noticed that in the normal regime (V_{CE}<0.3V), the collector current increases progressively with V_{CE} due to the purely resistive behavior of the transistor's. However, when the voltage increases (0.3V<V_{CE}<3V), the current I_C is minimally depended to V_{CE}, indicating current saturation (saturation zone). At height value of collector-emitter voltage (V_{CE}>3V), the current I_C increases slightly instead of stabilizing indicating the beginning of the Kirk effect.

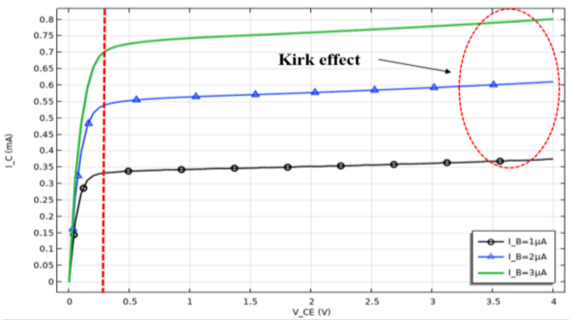

Fig. (4) Variation of collector current I_C as a function of V_{CE} for different base current I_B

3.2. Dynamic Characteristics

Due to the application of HBTs in the THz domains, our focus is on their dynamic performances, specifically the transition frequency f_t and maximum oscillation frequency f_{max}. These frequencies are described by the following equations:

$$f_t = \frac{1}{2\pi\left(\tau_f+\frac{KT}{qI_C}(C_{BC}+C_{BE})+(R_C+R_E).C_{BC}\right)} \quad (16)$$

$$f_{max} = \frac{f_t}{\sqrt{(8\pi R_B C_{BC})}} \quad (17)$$

The transition frequency f_t depends on various parameters including base-collector capacitance, emitter-base capacitance, transit time and resistances of the collector, emitter and base: C_{BC}, C_{BE}, τ_f, R_C, R_E and R_B, respectively. Whereas, f_{max} varies inversely with the base-collector capacitance C_{BC} and base resistor R_B, which in turn is inversely proportional to the base doping N_{ab} [22].

The 28-nm FD-SOI technology is considered a promising solution to overcome the limitations of the DPSA-SEG architecture employed in BiCMOS55 technology and also to improve frequency performance. This part presents a comparison of frequency f_t and f_{max} of both technologies, COMSOL simulations results are presented in Fig. (5). The moving from BiCMOS55 to FD-SOI 28 nm leads to an increase in frequency performance specifically the maximum frequency f_{max}, confirming the effectiveness of the EXBIC architecture in reducing base resistance and capacitance.

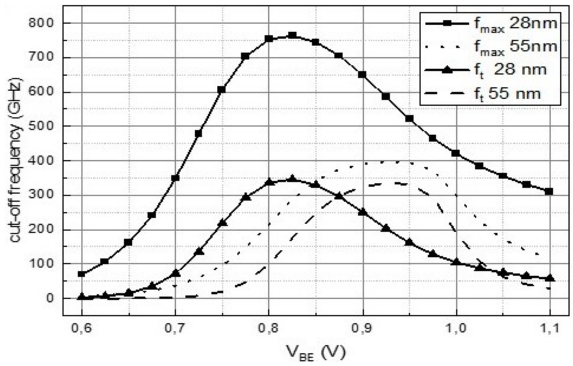

Fig. (5) Variation of f_t and f_{max} as a function of V_{BE} for both technologies FD-SOI 28nm and BiCMOS55 simulated using COMSOL software [23]

To validate our results, a comparative analysis was carried out using TCAD simulation data and experimental results available in the literature (Fig. 6). Table (2) summarizes the outcomes, the 28-nm FD-SOI technology achieves, at base-emitter voltage of 0.83V, a value of 346 GHz and 763.35 GHz for f_t and f_{max}, respectively. These values are comparable to those obtained by Vu et al. [12], which indicates f_t/f_{max}=380/780 GHz. In comparison, a value of f_t/f_{max} = 334/397 GHz has been obtained for BiCMOS55 using COMSOL software [23], which are close similar to TCAD simulation results reported in [11], which indicate f_t/f_{max} = 320/380 GHz. The minor deviations observed between our results and previously published work can be attributed to several modeling assumptions, such as idealized doping profile and simplified interface characteristics. The idealized doping profile corresponds to the use of an abrupt and uniform doping concentration (box profile type) in base and emitter region of the HBT, without accounting for diffusion effects. The simplified interface characteristics indicate that phenomena such us interface traps and surface roughness are neglected in our simulation. Furthermore, parasitic effects such as layout-induced capacitance and packaging-related effects were not explicitly taken into account in this study.

Table (2) Comparison between f_t and f_{max} of both technologies FD-SOI28 and BiCMOS55

Technology	f_t (GHz)	f_{max} (GHz)	Reference
28-nm FD-SOI	346	763.35	This work
28-nm FD-SOI	380	780	[27]
BiCMOS55	320	380	[11]
BiCMOS55	334	397	[23]

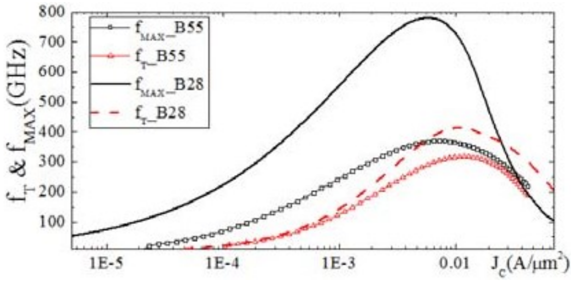

Fig. (6) Variation of f_t and f_{max} with the variation of collector current density for FD-SOI 28 nm and BiCMOS55 technologies using TCAD simulation by STMicroelectronics[27]

4. Optimization of Technological Parameters of FD-SOI 28nm Technology

4.1. Effect of Germanium Concentration

To investigate the influence of germanium content x in the $Si_{1-x}Ge_x$ alloy on transistor operation and frequency performance, simulations were performed for various germanium concentrations (10%, 20%, and 30%). As shown in figures (7) and (8), both the base and collector currents increase proportionally with increasing germanium concentration, leading to a significant enhancement in the static current gain β, which reaches a peak value of 3855 at x=30% (Table 3). This increase in current is primarily attributed to a reduction in the potential barrier encountered by electrons moving from the emitter to the base, which explains the increase in electron injection efficiency [24]. However, a decrease in f_t is observed, gradually from 352.2 to 337.8 GHz as the germanium concentration increases from 10% to 30% (Fig. 9). This degradation is mainly attributed to an increase in base transit time τ_B caused by the reduction in electron mobility due to increased alloy scattering within the base [25].

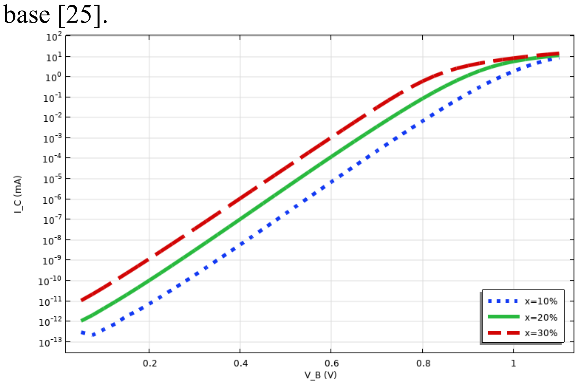

Fig. (7) Variation of I_C as a function of V_{BE} for different germanium concentration

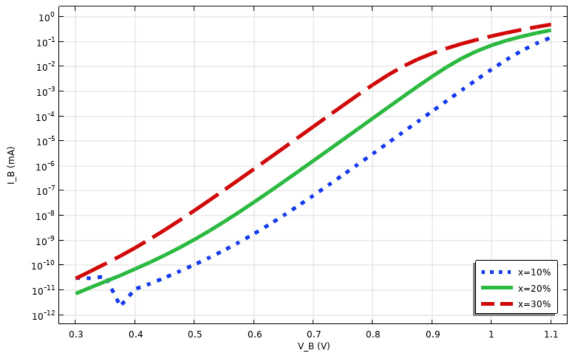

Fig. (8) Variation of I_B as a function of V_{BE} for different germanium concentration

Table (3) Static and dynamic performance for different germanium concentration x

x	I_C (mA)	I_B (mA)	β	f_t (GHz)	f_{max} (GHz)
10 %	$1.18x10^{-6}$	$3.2x10^{-10}$	3689	352.2	771.3
20 %	$2.19x10^{-5}$	$5.85x10^{-9}$	3742	345.9	763.35
30 %	$2.999x10^{-4}$	$7.79x10^{-8}$	3855	337.8	754.3

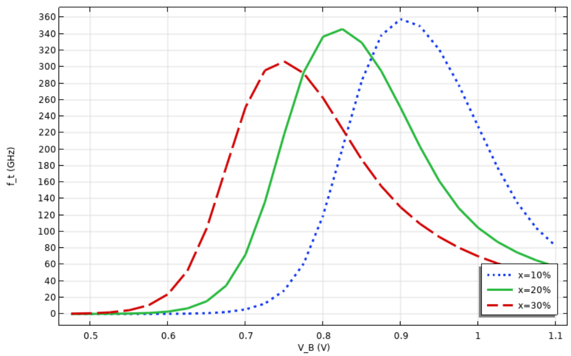

Fig. (9) Variation of f_t as a function of V_{BE} for different germanium concentration

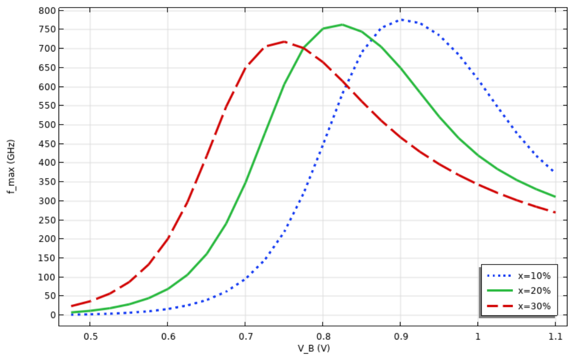

Fig. (10) Variation of f_{max} as a function of V_{BE} for different germanium concentration x

These results are in good agreement with those reported by Derrickson et al. [26], where the peak value of f_t is achieved at lower germanium concentration. The frequency f_{max} decreases with the decrease of f_t, dropping from 771.3 to 754.3 GHz (Fig. 10). The electron and hole mobility increase at high Ge concentration (>85%) explaining that as the germanium concentration increase the SiGe alloy becomes as Ge-type and its physical properties become closer to those of germanium than silicon [25].

4.2. Effect of Extrinsic Base Doping

This section investigates the effect of increasing extrinsic base doping N_{ab} on the electrical properties of the 28nm FD-SOI. The primary goal of this approach is to enhance the maximum oscillation frequency f_{max} by reducing the base resistance R_B, which made up of extrinsic base resistance R_{Ex} and intrinsic base resistance R_{SiGe}, as shown in the following equations:

$$R_B = R_{EX} + R_{SiGe} \quad (18)$$

$$R_{EX} = \frac{1}{q.N_{ab}.\mu_{ppoly}} \cdot \frac{2.L_{Bpoly}}{d_{Bpoly}.l_{HBT}} + \frac{1}{q.N_{ab}.\mu_{ppoly}} \cdot \frac{2.L_{Blink}}{d_{Blink}.l_{HBT}} \quad (19)$$

$$R_{SiGe} = \frac{1}{q.N_{BSiGe}.\mu_{pSiGe}} \cdot \frac{L_{BSiGe}}{d_{BSiGe}.l_{HBT}} \quad (20)$$

N_{BSiGe}, N_{ab} are the intrinsic and extrinsic base doping. μ_{ppoly}, μ_{pSiGe} are their hole mobility. L_{BSiGe}, L_{Bpoly}, L_{Blink} are base width of intrinsic, poly base and base link, respectively. d_{BSiGe}, d_{Bpoly}, d_{Blink} are their base depth and l_{HBT} is the length of the HBT. The coefficient 2 corresponds to the two extrinsic bases used in the EXBIC architecture (see Fig. 1).

Table (4) shows static and dynamic characteristics as a function of N_{ab}. As the doping increases from $4x10^{19}$ to $9x10^{20}$ cm^{-3}, the space charge region becomes narrower, which increases carrier recombination within the base, leading to an increase in I_B while a slight decrease in I_C is obtained [26]. The observed current variations result in a slight decrease in β from 3742 for a concentration of $4x10^{20}$ cm^{-3} to 3697 for a concentration of $9x10^{20}$ cm^{-3}.

Table (4) Electric characteristics for different extrinsic base doping N_{ab}

N_{ab} (cm^{-3})	$4x10^{19}$	$8x10^{19}$	$5x10^{20}$	$7x10^{20}$	$9x10^{20}$
R_E (Ω)	0.851	0.851	0.851	0.852	0.852
R_B (Ω)	217.17	188.17	163,8	162,48	161.74
C_{BC} (fF)	0.109	0.109	0.109	0.109	0.109
C_{BE} (fF)	0.1589	0.1589	0.1589	0.159	0.159
β	3742	3734	3721.7	3714	3697
f_t (GHz)	345.96	345.9	345.8	345.76	345.75
f_{max} (GHz)	763.35	820	878.72	882.27	884.26

The frequency f_t is not noticeably changed with the increased doping due to the minor reduction in the internal width of the transistor (Fig. 11). A notable decrease in R_B is observed, due to a decrease in both the poly silicon base and base link resistances. C_{BC} remains unchanged. Consequently, f_{max} increases to 884.26 GHz for a doping of $9x10^{20}$ cm^{-3} (Fig. 12). Our results confirm the findings of [27], where f_{max} reached a value of 835 GHz for a concentration of $8x10^{20}$ cm^{-3}.

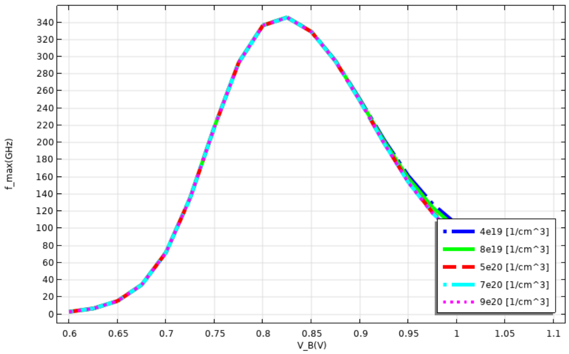

Fig. (11) Variation of the transition frequency f_t as a function of extrinsic base doping N_{ab}

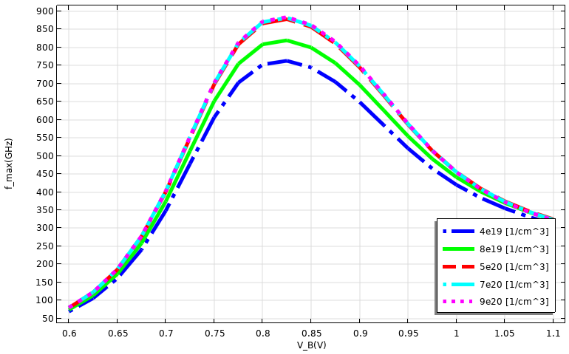

Fig. (12) Variation of the maximum frequency f_{max} as a function of extrinsic base doping N_{ab}

4.3. Effect of Emitter Height

In this section, we examine the impact of emitter height d_E on the electric characteristics of the FD-SOI 28 nm, using a germanium content of 20 % and fixed extrinsic base doping of $9x10^{20}$ cm^{-3}. As shown in table (5), reducing d_E by 20% results in a decrease in β from 3697 to 2817, due to a slight increase in I_B by the recombination processes at the emitter [28].

Table (5) Static and dynamic characteristics for different emitter height d_E

Emitter height (nm)	d_E	0.95 d_E	0.9 d_E	0.8 d_E
R_E (Ω)	0.851	0.893	0.942	1.071
R_B (Ω)	161.74	161.74	161.74	161.74
C_{BC} (fF)	0.109	0.109	0.109	0.109
C_{BE} (fF)	0.1589	0.1542	0.1495	0.1399
β	3697	3687	3583	2817
f_t (GHz)	345.95	354	359	360
f_{max} (GHz)	884.26	897.45	903.6	906

Furthermore, a slight increase in f_t from 345.75 to 360 GHz is observed (Fig. 13). This enhancement is due to a decrease in base-emitter capacitance C_{BE} accompanied by a significant reduction in emitter transit time τ_E, which in turn decreases the total transit time τ_f (Eq. 21 and 22). The decrease in τ_E is due to a decrease in the distance that carriers crossed from the emitter to the base. The slight increase of R_E (≈ 0.20 Ω) is considered negligible relative to the more substantial change of τ_E. R_B and C_{BC} remain unchanged. As a result, the increase in f_t contributes to an improvement in f_{max} from 884 GHz to 900 GHz (Fig. 14).

$$\tau_E = \frac{(3d_E)^2}{2\beta D_{pE}} \quad (21)$$

$$\tau_f = \tau_E + \tau_{BC} + \tau_B \quad (22)$$

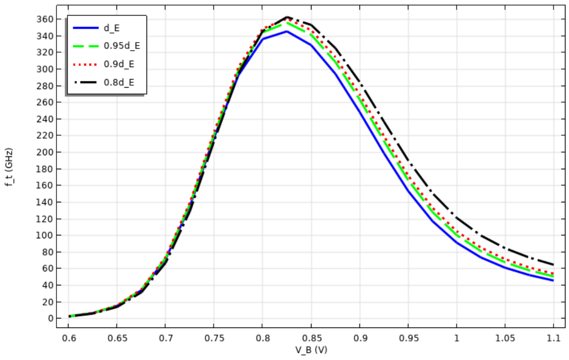

Fig. (13) Variation of the frequency f_t as a function of V_{BE} for different emitter height d_E

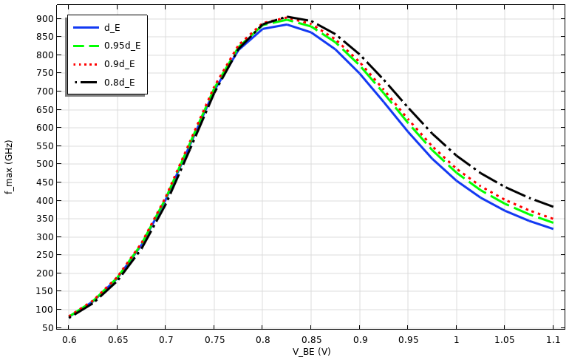

Fig. (14) Variation of the frequency f_{max} as a function of V_{BE} for different emitter height d_E

4.4. Effect of Emitter Width

Table (6) presents the electrical characteristics as a function of emitter width w_{fd}, using a germanium percentage of 20% and a base doping of $4x10^{19}$ cm^{-3}. The results show that decreasing the emitter width leads to a slight reduction in both β and f_t. The latter results from a small reduction in the collector current I_C and the base-emitter capacitances C_{BE}, accompanied with a significant rise in the emitter resistance R_E. However, f_{max} improves as a result of the decrease in base resistance R_B, reaching a value of 903.5 GHz when the emitter width is reduced by 20 %. These results are in accordance with those reported in [27], which mentioned that reducing emitter width leads to a decrease in current gain and transition frequency, while the maximum frequency is enhanced as the width is reduced.

5. Conclusion

The work discussed in this article focuses specifically on the electrical characteristics of a SiGe HBT integrated in FD-SOI 28 nm technology, using EXBIC architecture. This architecture offers two key features: oxide sidewalls isolate the extrinsic base from the collector and reduce C_{BC}, while the epitaxial boron in-situ-doped lateral base link reduces R_B. Electrical performance simulation of the FD-SOI 28nm showed values of 346 and 760 GHz for f_t and f_{max}, respectively. To enhance both f_t and f_{max}, a combination of high extrinsic base doping N_{ab} and a reduction in emitter height d_E is necessary. A large emitter width w_{fd} increases significantly R_B leading to reduce f_{max} while f_t benefits from this expansion. Optimal values of the above mentioned increased significantly the value of f_t and f_{max} to 360 GHz and 0.9 THz, respectively. This improvement in the frequency performance may lead to a better implementation of such HBT technologies in terahertz applications.

Table (6) Transistor electric performances for different emitter width w_{fd}

Emitter width (nm)	w_{fd}	0.95 w_{fd}	0.9 w_{fd}	0.8 w_{fd}
R_B (Ω)	217.17	213.81	211.02	206.21
R_E (Ω)	0.852	0.868	0.872	0.873
C_{BC} (fF)	0.109	0.109	0.109	0.109
C_{BE} (fF)	0.1589	0.1587	0.1585	0.1581
β	3697	3681	3618	3556
f_t (GHz)	345.96	341.2	340	336.5
f_{max} (GHz)	884.26	887.85	894.5	903.5

References

[1] F. Aniel et al., **"Terahertz Electronic Devices"**, Springer Handbook of Semiconductor Devices, (2023) pp. 807-849.

[2] T. Zimmer, "Recherche et évaluation d'une nouvelle architecture de transistor bipolaire à hétérojonction Si/SiGe pour la prochaine génération de technologie BiCMOS", France (2016).

[3] P. Chevalier et al., "SiGe BiCMOS current status and future trends in Europe", *IEEE BiCMOS and Compound Semiconductor Integrated Circuits and Technology Symposium BCICTS, IEEE (2018).*

[4] H. Ghanem et al., "Modeling and analysis of a broadband Schottky diode noise source up to 325 GHz based on 55-nm SiGe BiCMOS technology", *J. Trans. Microwave Theory Tech.*, 68(6) (2020) 2268-2277.

[5] J. Gonçalves et al., "Millimeter-wave noise source development on SiGe BiCMOS 55-nm technology for applications up to 260 GHz", *IEEE Trans. Microwave Theory Tech.*, 67(9) (2019) 3732-3742.

[6] B. Saha et al., "Sub-THz and THz SiGe HBT electrical compact modeling", *J. Electron.*, 10(12) (2021) 1397.

[7] E. Brezza et al., "Optimized emitter-base interface cleaning for advanced Heterojunction Bipolar Transistors", *J. Solid-State Electron.*, 204 (2023) 108654.

[8] A. Banerjee, "Basic Heterogeneous Bipolar|Bijunction Transistor (HBT) Properties", Semiconductor Devices: Diodes, Transistors, in **Solar Cells, Charge Coupled Devices and Solid State Lasers**, (2023), pp. 61-70.
[9] A. Pawlak, B. Heinemann and M. Schroter, "Physics-based modeling of sige HBTs with fj of 450 GHz with HICUM Level 2", *IEEE Bipolar/BiCMOS Circuits and Technology Meeting (BCTM), IEEE* (2017).
[10] C.E.G. Lachkhab et al., "COMSOL simulation of a new generation of SiGe heterojunction bipolar transistor (HBT) integrated in a BiCMOS 55nm technology", *AIP Publishing LLC* (2021).
[11] P. Chevalier et al., "Nanoscale SiGe BiCMOS technologies: From 55 nm reality to 14 nm opportunities and challenges", *IEEE Bipolar/BiCMOS Circuits and Technology Meeting-BCTM, IEEE (2015).*
[12] T. van Vu, "Recherche et évaluation d'une nouvelle architecture de transistor bipolaire à hétérojonction Si/SiGe pour la prochaine génération de technologie BiCMOS", France (2016).
[13] T. Zimmer et al., "SiGe HBTs and BiCMOS technology for present and future millimeter-wave systems", *IEEE J. Microwaves*, 1(1) (2021) 288-298.
[14] N. Miao et al., "Design and Simulation of Improved SOI SiGe Heterojunction Bipolar Transistor Architecture with Strain Engineering", *J. Appl. Math. Phys.*, 8(02) (2020) 218.
[15] A. Gauthier, "Study and development of a new Si/SiGe heterojunction bipolar transistor architecture compatible with FD-SOI CMOS technology", France (2019).
[16] S. Panda et al., "A TCAD-Based Analysis of Substrate Bias Effect on Asymmetric Lateral SiGe HBT for THz Applications", *IEEE Trans. Electron Dev.*, 70(5) (2023) 2192-2198.
[17] M. Schröter et al., "SiGe HBT technology: Future trends and TCAD-based roadmap", *Proceed. IEEE,* 105(6) (2016) 1068-1086.
[18] A. Boulgheb, M. Lakhdara and S. Latreche, "Improvement of the Self-Heating Performance of an Advanced SiGe HBT Transistor Through the Peltier Effect", *IEEE Trans. Electron Dev.*, 68(2) (2021) 479-484.
[19] K. Petrosyants and R. Torgovnikov, "Electro-thermal modeling of trench-isolated SiGe HBTs using TCAD", *31st Thermal Measurement, Modeling & Management Symposium (SEMI-THERM), IEEE (2015)*.
[20] N.D. Arora, J.R. Hauser and D.J. Roulston, "Electron and hole mobilities in silicon as a function of concentration and temperature", *IEEE Trans. Electron Dev.*, 29(2) (1982) 292-295.
[21] C.T. Kirk, "A Theory of Transistor Cutoff Frequency (f T) Falloff at High Current Densities", *Semiconductor Devices: Pioneering Papers*, (1962) 260-270.
[22] S. Kong et al., "Effect of uniaxial strain on characteristic frequency of scaled SiGe HBT with embedded stress raiser", *J. Comput. Electron.*, 21(5) (2022) 1116-1126.
[23] C.E.G. Lachkhab et al., "Optimisation of extrinsic base doping of a SiGe heterojunction bipolar transistor integrated in a BiCMOS 55 nm technology for high frequency performances", *Int. J. Nanotech.*, 20(11/12) (2023) 1017.
[24] M. Lakhdara et al., "Optimization of abrupt profile of germanium in Si/SiGe heterojunction bipolar transistor specified for radio frequency range systems", *J. Appl. Mech.*, 492 (2014) 316-320.
[25] D. Bae and B. Choi, "Demonstration of a high-performance SiGe alloy channel considering Ge fraction, Dit and BTB leakage", *J. Electron. Lett.*, 55(20) (2019) 1106-1108.
[26] A. Derrickson et al., "Assessment of THz performance for a lateral SiGe HBT on SOI with a laterally graded base", *IEEE Trans. Electron Dev.*, 65(11) (2018) 4747-4754.
[27] T. van Vu et al., "Advanced Si/SiGe HBT architecture for 28-nm FD-SOI BiCMOS", *Bipolar/BiCMOS Circuits and Technology Meeting (BCTM), IEEE (2016).*
[28] B. Barbalat et al., "Experimental study of metallic emitter SiGeC HBTs", *Bipolar/BiCMOS Circuits and Technology Meeting, IEEE (2006)*.